# Numerical Investigation of Turbulent Flow around a Rotating Stepped Cylinder for Corrosion Study

## Kyung-Soo Yang[1]*, Jong-Yeon Hwang[1], Klaus Bremhorst[2] and Srdjan Nesic[2#]

[1] *Department of Mechanical Engineering, Inha University, Incheon, 402-751, Korea*
[2] *Department of Mechanical Engineering, The University of Queensland Brisbane, Qld 4072, Australia*

Complex flows with boundary layer separation and reattachment commonly occur in situations of practical interest. In such flows, any accompanying heat or mass transfer is strongly influenced by the fluid dynamics. For example, rates of heat or mass transfer to the wall can have large variations in the reattachment region. In the case of heat transfer, a practical example is local overheating downstream of a heat exchanger pipe fitting. When it comes to mass transfer, accelerated metal loss is often encountered downstream of flow disturbances due to enhanced mass-transfer-controlled corrosion (Postlethwaite, 1986; Mahato et al., 1968; Nesic and Postlethwaite, 1990). This phenomenon is often termed flow-accelerated corrosion or erosion-corrosion and is most severe in complex flow situations, for example, at heat exchanger tube inlets (Elvery and Bremhorst, 1997; Elvery and Bremhorst, 1996), pipe bends, downstream of orifice plates, valves, fittings, weld beads and in turbo-machinery including pumps, turbines and propellers (Postlethwaite and Nesic, 2000). In all of these cases, increased turbulent transport in the near-wall region enhances mass-transfer rates of species involved in the corrosion reaction. Most of the time these are anionic species which are consumed by the corrosion reaction at the metal surface and need to be replenished by the transport from the bulk. In other cases, they are products of protective film (scale) dissolution which are swept away from the surface leading to more rapid film removal and accelerated corrosion attack.

In a recent study, a new compact experimental setup was tested for study of erosion-corrosion under disturbed flow conditions, involving a rotating cylinder geometry with two axisymmetrically-mounted sudden steps (Nesic et al., 2000). It is believed that this geometry can become a simple and effective tool for studying erosion-corrosion under disturbed flow conditions and substitute much more complex and expensive flow-loop based systems. Initial characterization of the stepped rotating cylinder electrode was conducted, involving wall heat/mass-transfer measurements (Nesic et al., 2000; Bienkowski, 1998). The measured variation in the heat and mass-transfer rates behind the step suggested that a complex flow pattern was created which would most likely lead to a variation in the erosion-corrosion rate. Due to the small size and curved shape of the flow geometry, detailed measurements of the flow parameters downstream of the step were difficult. Therefore, flow simulations were undertaken and these are reported below.

Direct numerical simulation has been carried out for turbulent flow set up by a rotating cylinder with two backward-facing steps axisymmetrically mounted in the circumferential direction. This flow geometry creates a qualitatively similar flow pattern as observed near a sudden pipe expansion or a plane backward-facing step, characterized by flow separation and reattachment. A region of intense turbulence intensity and high wall-shear-stress fluctuations is formed in the recirculating region downstream of the step, where high mass-transfer capacity was also experimentally observed. Since corrosion is frequently mass-transfer controlled, our findings put forward this apparatus as a useful tool for future corrosion research.

On a effectué une simulation numérique directe de l'écoulement turbulent créé par un cylindre rotatif ayant deux contractions axisymétriques dans la direction circonférentielle. Cette géométrie crée un profil d'écoulement qualitativement similaire à celui qu'on observe près d'une expansion de conduite soudaine ou d'une contraction planaire, caractérisés par la séparation et le ré-attachement de l'écoulement. Une région d'intense turbulence et de fortes fluctuations de contraintes de cisaillement pariétal se forment dans la région en recirculation en aval de la contraction, où une grande capacité de transfert de matière a également été observée expérimentalement. Étant donné que la corrosion dépend souvent du transfert de matière, nos résultats font la promotion de cet appareillage en tant qu'outil utile pour la recherche future sur la corrosion.

**Keywords:** corrosion, backward-facing step, turbulence, mass transfer, direct numerical simulation.

With rapid progresses in developing fast computers and efficient numerical algorithms achieved in recent years, direct numerical simulation (DNS) can provide accurate flow data for well-defined flow problems with moderate turbulence (Härtel, 1996). Thus, the numerical results obtained by DNS can be regarded supplementary to experimental studies, and used in identifying related flow physics. In this work, DNS has

been carried out for turbulent flow around a rotating cylinder with two backward-facing steps axisymmetrically mounted in the circumferential direction. The cross-section of the cylinder is exactly the same as that of the experimental apparatus used in the previous corrosion study (Nesic et al., 2000; Bienkowski, 1998). The aim of this paper is to elucidate the flow characteristics associated with this particular configuration, and to provide detailed flow data for researchers in the field of erosion-corrosion. The results obtained also suggest the practical applicability of the stepped rotating cylinder as an economic and tractable tool for corrosion research.

## Formulation

In this study, computations were carried out with respect to a reference frame rotating with a constant angular velocity ($\Omega$). The governing incompressible continuity and momentum equations are:

$$\nabla \cdot \mathbf{u} = 0 \tag{1}$$

$$\frac{\partial \mathbf{u}}{\partial t} + (\mathbf{u} \cdot \nabla)\mathbf{u} = -\frac{1}{\rho}\nabla P + \nu \, \nabla^2 \mathbf{u} \, - \, 2\Omega \times \mathbf{u} \tag{2}$$

where $\mathbf{u}$, $\rho$ and $\nu$ denote velocity, density, and kinematic viscosity, respectively. Turbulence modelling is not included; all scales are resolved using a fine grid. The last term in Equation (2) represents the Coriolis force. Since the centrifugal force is conservative, it is included in the pressure term, and does not affect the velocity field (Lezius and Johnston, 1976). Thus $P$ in Equation (2) includes not only pressure but also the centrifugal potential. The governing equations were discretized using a finite-volume method in a generalized coordinate system. Spatial discretization is second-order accurate. A hybrid scheme is used for time advancement; nonlinear terms and cross diffusion terms are explicitly advanced by a third-order Runge-Kutta scheme, and the other terms are implicitly advanced by the Crank-Nicolson method. A fractional step method (Rosenfeld et al., 1994) is employed to decouple the continuity and momentum equations. The Poisson equation resulting from the second stage of the fractional step method is solved by a multigrid method. During the process of solving the Poisson equation, iteration continues until the sum of the absolute residual of each control volume reaches the level of machine error in order to enforce the continuity. For the details of the numerical algorithm used in the code, see Rosenfeld et al. (1994). Unless specified otherwise, all the flow variables are normalized by the step height ($h$) and the circumferential speed of the cylinder surface upstream of the step ($U_0$) as the length and velocity scales, respectively.

## Choice of Numerical Parameters

Simulation was performed with a rotation rate of $\Omega = 2000$ rpm in air; this corresponds to $Re = 335$ where $Re$ represents a Reynolds number based on $U_0$ and $h$. Although air rather than water was used for the present simulations, the velocity field is unaffected as geometric similarity is maintained, both air and water are Newtonian, both fluids are incompressible at the speeds in question and Reynolds number similarity is applied.

The shape of the cylinder cross-section was taken exactly the same as that of the central part of the cylinder in the experiment (Nesic et al., 2000; Bienkowski, 1998). A schematic diagram is
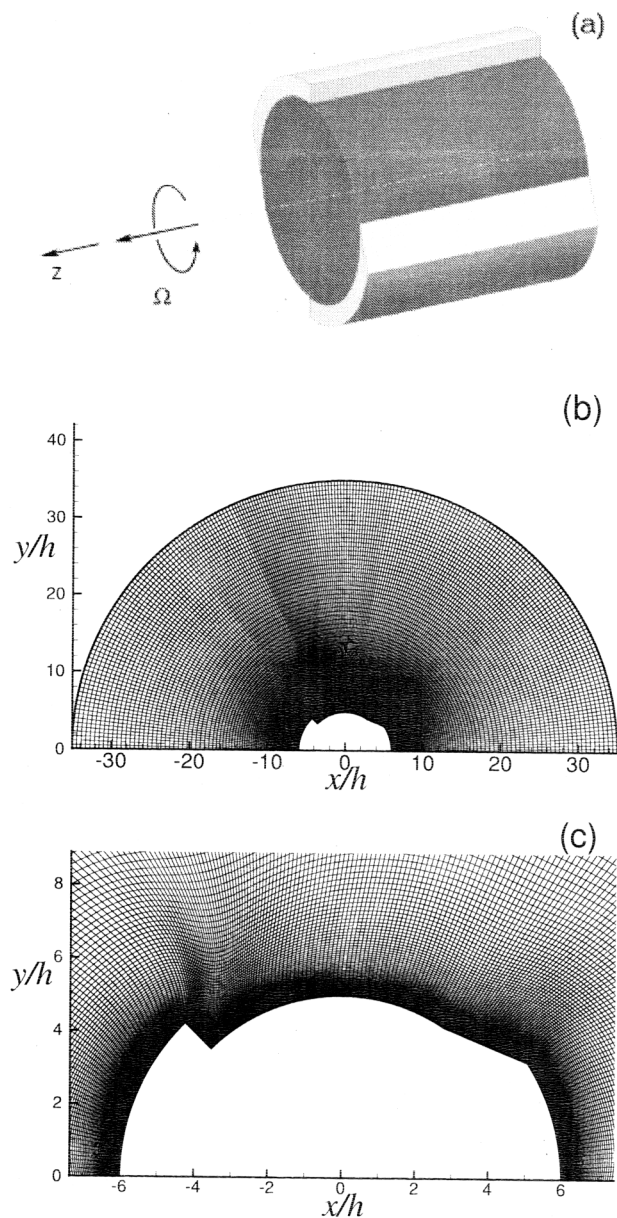


**Figure 1.** A schematic diagram and the grid system at a cylinder cross-section: (a) Schematic; (b) total view; (c) magnified view.

shown in Figure 1a. Since the steps are mounted axisymmetrically with respect to the axis of rotation, only one half of the domain is considered, thus allowing double the numerical resolution in the circumferential direction. Periodic boundary conditions were used, as turbulent length scales were found to be shorter than the distance between the boundaries with two point spatial correlations of fluctuating velocities decreasing to zero well before any domain boundary is reached. The spanwise (axial) direction ($z$) is assumed as homogeneous. In fact, a test simulation with the entire flow domain revealed no subharmonic structures and the averaged velocity field was axisymmetric with respect to the axis of rotation.

The outer boundary of the computational domain is located approximately three diameters (0.07 m) away from the center

of rotation, and the spanwise size ($W$) of the domain is one diameter (0.024 m). The step height is 0.002 m. The computational grid employed in this study is shown in Figure 1. Figure 1b exhibits the whole computational domain at one cross-section in the spanwise direction, and Figure 1c is a magnified view around the cylinder. The grid is a body-fitted O-grid system which is the most suitable for this complicated geometry, with more resolution near the step and solid boundaries. The number of grid points was progressively refined using grid-refinement study up to $224 \times 128 \times 80$ in the circumferential, normal, and spanwise directions. Based on the friction velocity $u_\tau$ at the location $3h$ upstream of the step, the minimum and maximum grid spacing in each direction is $\Delta^+_{min} = 0.0174$, $\Delta^+_{max} = 3.18$ in the circumferential direction, $\Delta^+_{min} = 0.0086$, $\Delta^+_{max} = 0.67$ in the normal direction, and $\Delta^+_z = 4.7$ in the spanwise direction, respectively. One typical run including statistical evaluation takes about 12 000 time steps which correspond to 10 revolutions of the cylinder, and one time step takes approximately 50 s on a CRAY C90 supercomputer.

## Initial and Boundary Conditions

With respect to the rotating reference frame, the inner cylinder is stationary while the outer circular boundary is rotating in the clockwise direction. The initial flow field was constructed such that at any location in the flow field, the velocity was given as $\Omega$ times the distance between the point and the center of rotation. This is an obvious choice because in the laboratory the cylinder starts rotating counter-clockwise in stationary ambient fluid. In addition, a small-amplitude random noise of which root-mean-squared magnitude was approximately 0.1% of $U_0$ was added only at the beginning of the simulation in order to bypass the transitional regime and establish a self-sustaining turbulence as quickly as possible.

The no-slip boundary condition was applied on the surface of the cylinder and a periodic boundary condition was employed in the homogeneous spanwise direction. The outer boundary condition needs special attention. One could impose a constant circumferential speed of $\Omega r_0$, where $r_0$ is the outer radius of the domain, on the outer boundary. This corresponds to the situation that the outer boundary is located far way from the cylinder such that the air at the outer boundary is not disturbed by the motion of the cylinder. From the numerical point of view, this requires a large computational domain with a fine resolution near the outer boundary which is not the region of our interest. This will result in a significant waste of computational resources. To minimize this, a proper boundary condition was devised and employed on the outer boundary. That is,

$$\frac{\partial v_\theta}{\partial n} = \Omega, \qquad v_r = 0, \qquad \frac{\partial v_z}{\partial n} = 0 \qquad (3)$$

where $v_\theta$, $v_r$ and $v_z$ represent the circumferential, normal, and spanwise velocity components, respectively, and $n$ denotes the direction locally perpendicular to the outer boundary. This boundary condition allows use of a reasonably small computational domain without significantly disturbing the flow field near the cylinder which is the region of primary interest. Furthermore, since the circumferential velocity gradient is exactly specified at the boundary, rather than computed during the simulation, a fine numerical resolution is not required near the outer boundary. This leads us to an additional saving in CPU time.

## Results and Discussion
### Average Velocity Fields
After the flow reached a statistically steady state, collecting instantaneous flow fields was initiated for statistical evaluation. Averaging of the flow variables was carried out in the homogeneous spanwise direction and also in time. More than 160 instantaneous flow fields were collected over seven revolutions of the cylinder.

The averaged streamlines in the vicinity of the step are shown in Figure 2. The main recirculating region and a secondary one near the corner can clearly be identified. Figure 2 confirms that this flow geometry will create a qualitatively similar flow pattern as observed near a sudden pipe expansion or a plane backward-facing step, including flow separation and reattachment. The mean reattachment point is located at $s/h = 4.9$ where $s$ is the coordinate axis along the cylinder surface as indicated in Figure 2. The mean reattachment length ($X_r$) is shorter than that of plane backward-facing step flow (PBSF) due to the curvature effect; Le et al. (1997) reported $X_r = 6.28h$ at Reynolds number 5100 based on the step height and inlet free-stream velocity.

The distributions of the averaged circumferential and spanwise wall-shear stresses ($\overline{\tau}_{w_s}$ and $\overline{\tau}_{w_z}$, respectively, where the overbar means averaging both in $z$ and in time) are shown in
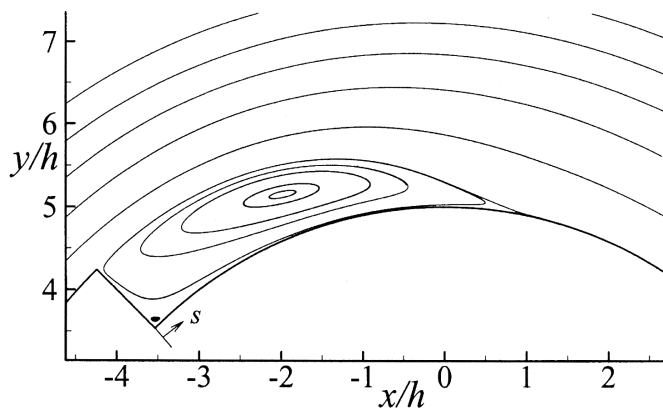


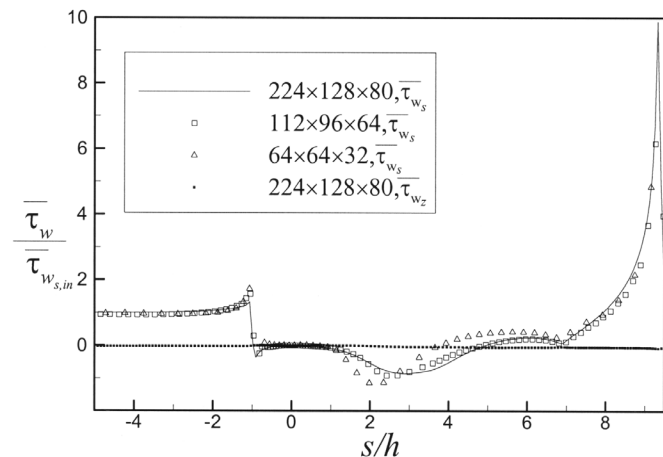**Figure 2.** Mean flow field near the step; streamlines.



**Figure 3.** Distribution of the mean wall-shear stress: $\overline{\tau}_{w_s}$, circumferential; $\overline{\tau}_{w_z}$, spanwise. The wall-shear stresses are normalized by an upstream $\overline{\tau}_{w_s}$ at $s/h = -4$ ($\tau_{w_s,in}$).
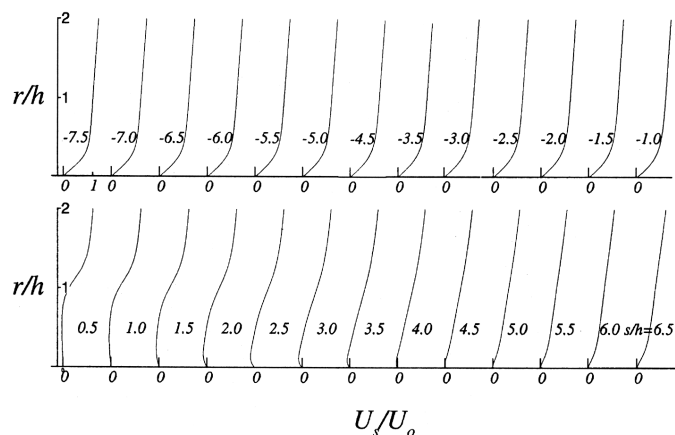
**Figure 4.** Profiles of the mean circumferential velocity component ($U_s$) at selected $s$ locations. Here, $r$ denotes the radial coordinate measured in the direction locally normal to the cylinder surface.



**Figure 5.** Distribution of the mean turbulence intensity near the step, normalized by $U_0$.

Figure 3. The wall-shear stresses are normalized by an upstream $\overline{\tau}_{w_s}$ at $s/h = -4$ ($\overline{\tau}_{w_s,in}$). The coarse-grid ($64 \times 64 \times 32$) results deviate considerably from those of the other finer grid computations ($112 \times 96 \times 64$, $224 \times 128 \times 80$) in terms of the shape of $\overline{\tau}_{w_s}$ distribution and the location of the reattachment point. Since the wall-shear stress is very sensitive to numerical resolution, Figure 3 indicates that the finest grid ($224 \times 128 \times 80$) is acceptable. The maximum magnitude of the averaged circumferential wall-shear stress ($|\overline{\tau}_{w_s}|_{max}$) is identified in the main recirculating region at $s/h = 2.9$; $\overline{\tau}_{w_s}$ vanishes downstream of the step at $s/h = 4.9$. The sharp peak at $s/h = 9.2$ corresponds to the corner in Figure 1c near $x/h = 5.1$. This is far downstream of the step and not in the region of main interest. The corner is needed to re-establish the flow for the step on the other side of the cylinder. Around $s/h = -4$, which corresponds to three step heights upstream of the sharp edge of the step (recall that the origin of $s$ is located at the concave corner of the step), $\overline{\tau}_{w_s}$ is nearly constant; $u_\tau$ at this location was employed for the normalization of grid spacing in wall units. The average spanwise wall-shear stress is nearly zero along the cylinder surface as it should be since the flow is homogeneous in the spanwise direction.

In Figure 4, profiles of the mean circumferential velocity component ($U_s$) are shown at selected $s$ locations; each profile represents the radial distribution of $U_s$ normalized by $U_0$. The main recirculating region is clearly seen, even though the shape of each profile is quite different from those in PBSF seen in Figure 17 of Le et al. (1997). With respect to the rotating reference frame, $U_s$ is increasing linearly in the radial direction as $r$ goes to infinity. One can also notice that the flow past the step is quickly re-established and approaches the next step with constant $\overline{\tau}_{w_s}$ as seen from the region $-5 \le s/h \le -3$. The secondary recirculating region is much smaller than the counterpart in the PBSF as seen from the profile at $s/h = 0.5$ and Figure 2 of this paper, and Figure 8 and the profile at $x/h = 0.5$ in Figure 17 of Le et al. (1997).

**Turbulence Intensity and Wall-Shear-Stress Fluctuation**
Turbulence in the near-wall region plays an important role of enhancing mass-transfer rates of species involved in corrosion reaction. In Figure 5, the mean turbulence intensity $I = \sqrt{u_i'u_i'/3}$
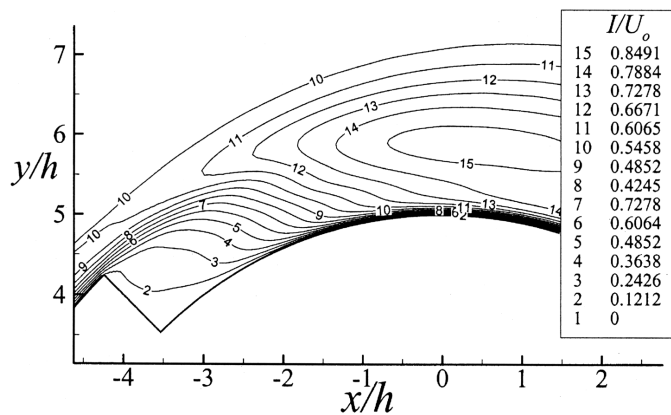
(where $u_i'$ is the velocity fluctuation in direction $i$) around the step is presented. Steep variations of $I$ in the direction perpendicular to the wall are noticed along the cylinder surface. Furthermore, the maximum of $I$ is observed one $h$ above the cylinder surface in the reattachment region.

**Comparison with Heat-transfer Measurements**
A hot film element embedded in an electrode was used to determine what effects the backward-facing step has on the heat transfer from the element as a function of distance behind the step. The hot-film measurements were carried out at 2000 rpm in air, thus yielding exactly the same $Re$ as in DNS. Surface heat transfer measurements were obtained with a 1 mm long platinum film mounted on the surface of the inner cylinder. The film gives a close approximation to the patch electrode used for mass transfer data described in the next section. Constant current heating was applied. Since the film output is sensitive to temperature and velocity or wall-shear-stress changes, calibration for both stimuli was undertaken. A temperature calibration was performed by operating the probe in an oven at different temperatures, thus giving the temperature sensitivity. Calibration of the film as a function of wall-shear stress, that is, rotational speed, was performed with the smooth cylinder by removing the outer sleeve. As an absolute velocity or wall-shear stress cannot be established for wall mounted films by independent means such as a Pitot tube calibration, measurements behind the step are taken relative to the probe output for the smooth cylinder. In locations where surface heat transfer behind the step is larger than for the smooth cylinder at the same rotational speed, a larger film output will be obtained than is the case for the smooth cylinder. Corresponding to this higher output, will be a smooth cylinder rotational speed giving the same probe output. This higher smooth cylinder rotational speed is the equivalent rpm. One can see Bienkowski (1998) for a detailed description of the experimental setup.

Although mass-transfer measurements are presented below, the hot-film measurements provide an independent path of studying flow physics related to the current flow configuration. In Figure 6, distribution of $I$ along the cylinder surface, computed at $0.006h$ away from the surface, is shown together with the hot film measurements (Bienkowski, 1998). Here,
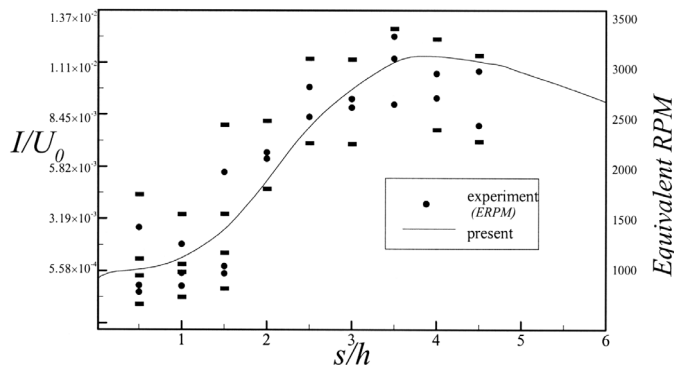
**Figure 6.** Distribution of the mean turbulence intensity along the cylinder surface, computed at 0.006$h$ away from the surface, shown together with the hot film measurements (Bienkowski, 1998) at 2000 rpm in air.



**Figure 7.** Distribution of the rms of wall-shear-stress fluctuation along with the hot-film measurements (Bienkowski, 1998).

equivalent RPM (ERPM) represents normalized values using those of the circular cylinder without the steps; a value larger (less) than 2000 ERPM means a higher (lower) heat-transfer rate than the no-step counterpart (Silverman, 1988) as explained above. The range between two small rectangles at a given $s$ indicates an error bar, and the small circles represent typical measurements at that $s$. The total error was evaluated as the sum of squares of errors with 95% confidence and includes the effect of slip-rings used to get the signal from the rotating cylinder to the stationary instruments, low signal-to-noise ratio of wall mounted hot-film gauges and calibration relative to the smooth rotating cylinder. Since $I$ and ERPM have different dimensions, quantitative comparison cannot be made. Nevertheless, qualitative comparison can be made regarding the trend of heat-transfer rate along the cylinder surface and the location of the maximum value. Figure 6 reveals that the computation predicts a wide range of high turbulence intensity ($3.5 \leq s \leq 4.5$) which is consistent with the experimental measurements; in this range of $s$, the mean turbulence intensity also has a steep normal gradient (Figure 5).

Fluctuation of wall-shear stress is another factor which is important in flow-accelerated corrosion. In Figure 7, the distribution of the computed root-mean-square (rms) of wall-shear-stress fluctuation along the cylinder surface is shown. Here, both the circumferential and the spanwise components are considered and plotted as well as the total, i.e.:

$$J = \sqrt{\overline{\tau_w'^2}} = \sqrt{\overline{\tau_{w_s}'^2} + \overline{\tau_{w_z}'^2}} \qquad (4)$$

In Figure 7, the distributions of the normalized heat-transfer rate obtained from the hot-film measurements (Bienkowski, 1998) are also shown. The computed data of $J$ match the experimental results well; this suggests that not only turbulence intensity but also wall-shear-stress fluctuation can significantly affect flow-accelerated corrosion. Other interesting features include that the rms of the wall-shear-stress fluctuation is of the same order or larger than the mean value (Figure 3) throughout the domain, and that the spanwise component ($\sqrt{\overline{\tau_{w_z}'^2}}$) is dominant in the range of maximum $J$. The latter will be given a more detailed explanation in the following section.

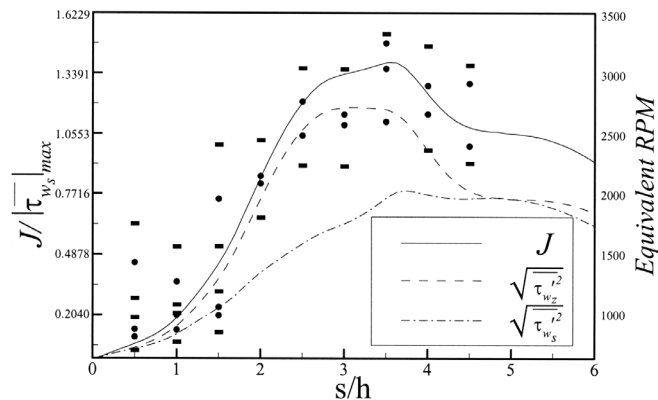### Comparison with Mass-transfer Measurements

In Figure 8, measurements of the mass-transfer rate downstream of the step are shown. In order to measure the local rates of mass transfer, electrochemical measurements were employed. A three-electrode electrochemical cell was used. A small circular flush mounted platinum probe which could be easily moved with respect to the step was used as a working electrode; a saturated Ag/AgCl reference electrode with a Luggin capillary provided the reference potential. The counter electrode consisted of a 80 mm diameter platinum ring which was placed concentrically around the rotating cylinder. Since the working electrode was small (0.7 mm in diameter) a fully developed mass-transfer boundary layer was not achieved. Therefore, the electrode had to be calibrated before each experiment in order to obtain a reference value without the step. The working solution was made by adding equimolar amounts of ferri and ferro cyanide and as well as potassium hydroxide which served as a supporting electrolyte. Concentration of ferro/ferri cyanide of 0.1 molar was used in order to obtain measurable currents on such small electrode. Potentiostatic measurements were made by holding the potential in limiting current region by using a potentiostat. The current was recorded and then converted into
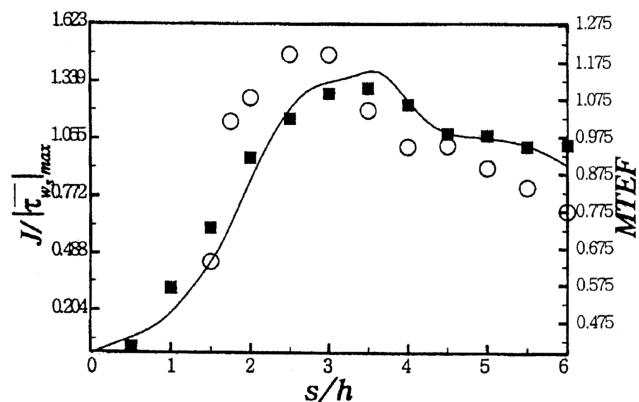


**Figure 8.** Distribution of the rms of wall-shear-stress fluctuation along with the mass-transfer measurements: —: DNS at $Re = 335$; ■: MTEF at $Re = 243$; ○: MTEF at $Re = 463$.
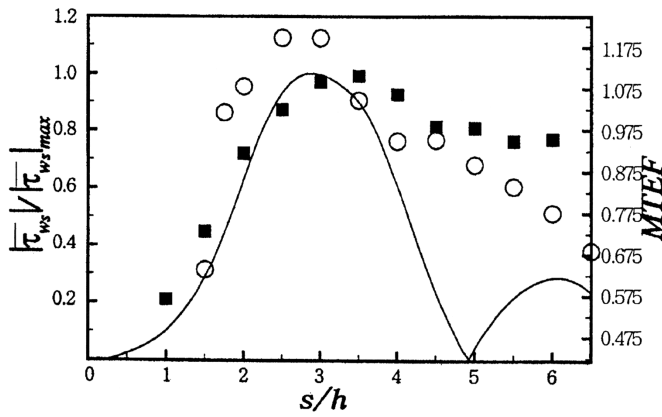
**Figure 9.** Distribution of the magnitude of mean wall-shear stress along with the mass-transfer measurements: —: DNS at $Re$ = 335; ■: MTEF at $Re$ = 243; ○: MTEF at $Re$ = 463.

the local mass-transfer coefficient. For detailed description of the experimental setup, see Nesic et al. (2000).

The measured mass-transfer rates were normalized by the reference values obtained without the step in order to obtain the, here-called, mass-transfer enhancement factor (MTEF) due to the disturbed flow geometry. In Figure 8, distributions of MTEF at $Re$ = 243 and $Re$ = 463 along the cylinder surface are plotted. For qualitative comparison, distribution of the normalized $J$ at $Re$ = 335 is also shown. The tendency of MTEF along the cylinder surface follows that of $J$ quite well. Locations of the maximum MTEF vary slightly depending on $Re$; the location of the maximum $J$ is in the range consistent with MTEF. This close correlation between MTEF and $J$ suggests that large unsteady flow structures as discussed below are primarily responsible for increased rates of wall mass transfer as suggested by Campbell and Hanratty (1983) and Calmet and Magnaudet (1997) for simple channel flow.

Mean wall-shear stress is a flow parameter often associated with mass-transfer-controlled erosion-corrosion (Silverman, 1988). In Figure 9, distribution of the magnitude of the wall-shear stress averaged both in time and in $z$ is shown along the cylinder surface, together with the mass-transfer measurements. It can be seen here that the often-quoted mean wall-shear stress is not correlated with the measured mass-transfer rate as it has a value of zero at the reattachment point. In reality there is no reattachment point; there is only a broad reattachment region arising from the large scale unsteadiness of the flow as discussed below.

### Instantaneous Velocity and Vortical Fields

The large-scale unsteadiness and three-dimensionality of the turbulent flow are illustrated in Figure 10. Figures 10a and 10b show the regions of instantaneous reversed flow at two different spanwise locations but at the same time, and Figures 10a and 10c at two different times approximately 2.7 revolutions apart but at the same spanwise location. The flow structures are quite different both in space and in time as one can expect in turbulent flows. The location of the instantaneous reattachment point of the main recirculating region varies considerably, up to approximately $3h$, in time and space as in a PBSF (Le et al., 1997). Figure 11 depicts the instantaneous reattachment points at a fixed $z$-location during three revolutions of the cylinder; the
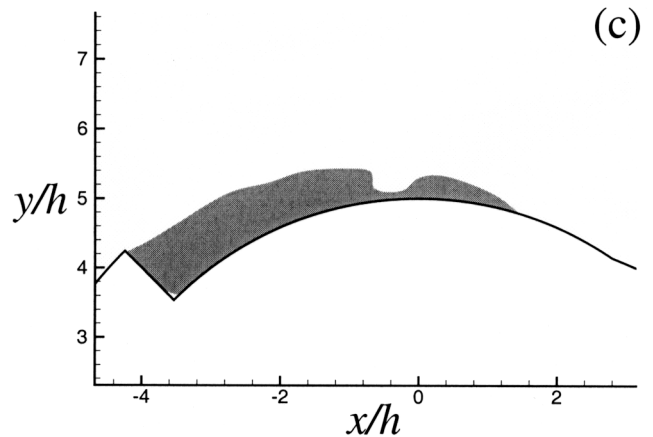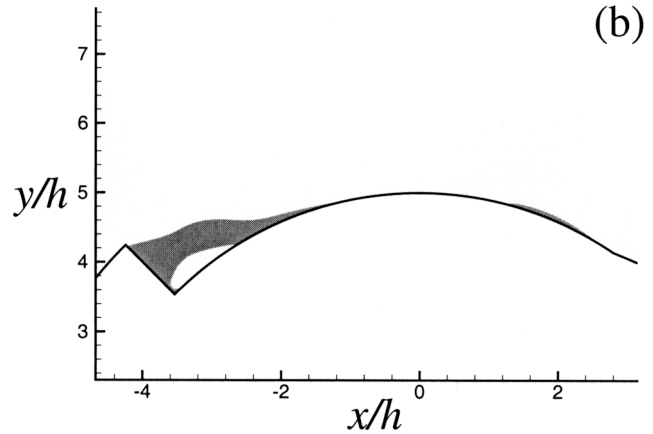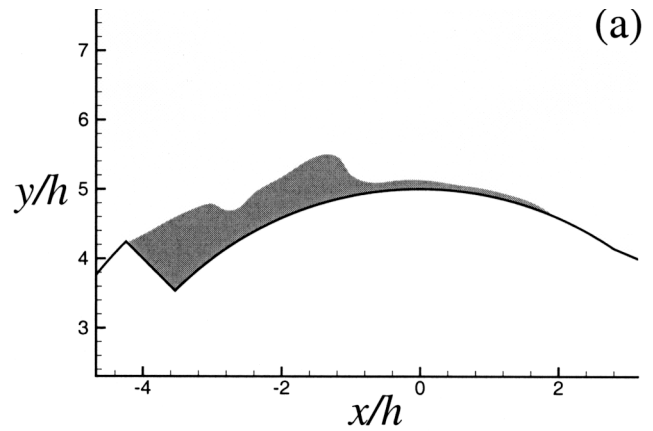


**Figure 10.** Regions of instantaneous reversed flow: (a) $z = z_1$, $t = t_1$; (b) $z = z_1 + W/2$, $t = t_1$; (c) $z = z_1$, $t = t_1 + 2.7T$ where $T$ is the period of the cylinder rotation.

symbols represent the reattachment points as identified by zero $s$-component of the wall-shear stress. It is seen that the recirculating region periodically stretches out on the cylinder surface; simultaneously it breaks into pieces (e.g. $1.0 \leq T \leq 1.2$, where $T$ is the period of the cylinder rotation). This explains why the hot-film (Figures 6 and 7) and mass-transfer (Figures 8 and 9) measurements have a smeared peak in the reattachement region.
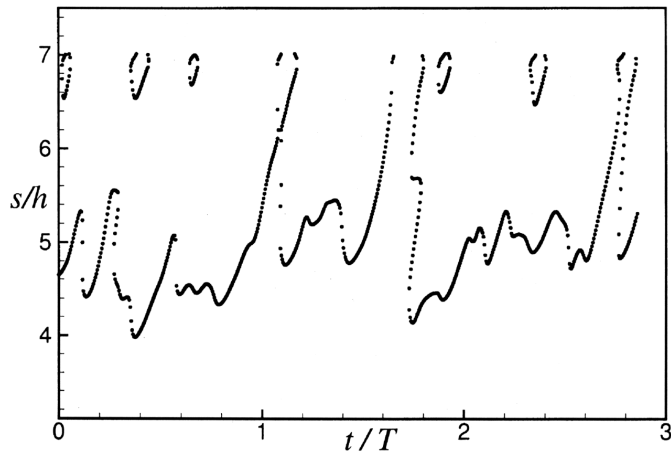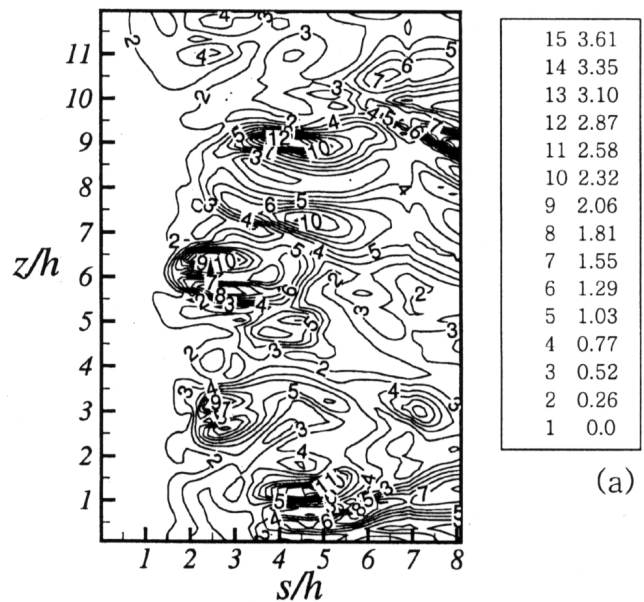
**Figure 11.** Instantaneous reattachment points on a typical spanwise (*x-y*) plane.



**Figure 12.** Magnitude contours of normalized instantaneous fluctuation of the wall-shear stress ($\sqrt{\tau_{w_s}'^2 + \tau_{w_z}'^2} / |\overline{\tau}_{w_s}|_{max}$) on the cylinder surface downstream of the step; (a) $t = t_1$, (b) $t = t_1 + 2.7T$.

In Figure 12, magnitude contours of normalized instantaneous fluctuation of the wall-shear stress ($\sqrt{\tau_{w_s}'^2 + \tau_{w_z}'^2} / |\overline{\tau}_{w_s}|_{max}$) on the cylinder surface downstream of the step are presented; Figures 12a and 12b correspond to Figures 10a and 10c, respectively in time. It can be noticed that the wall-shear stress varies significantly between $s/h = 2.0$ and $s/h = 5.0$, consistent with the peak ranges of heat/mass-transfer measurements. Furthermore, one can estimate that the maximum magnitude of the instantaneous wall-shear-stress fluctuation is three to four times larger than the maximum mean value (Figure 3). Such intense wall-shear stresses occur locally and intermittently.
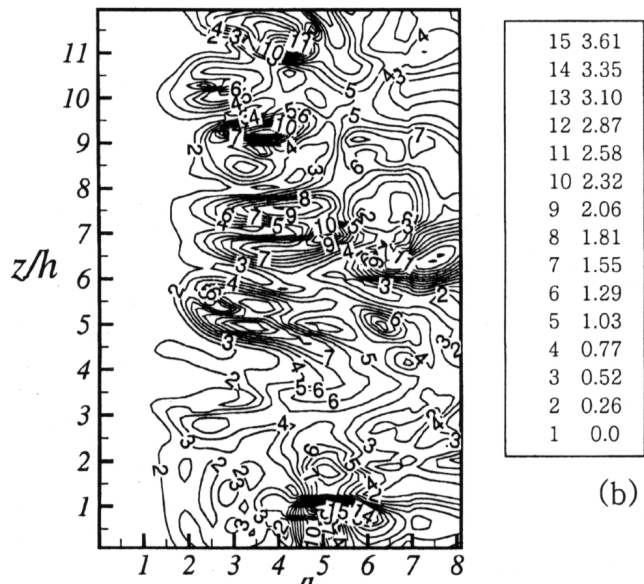
In Figure 13, contours of the instantaneous fluctuation of the circumferential velocity component ($u_s'$) at $0.006h$ away from the cylinder surface are shown. The solid lines represent positive values; the dashed lines indicate negative ones. Elongated, alternating positive and negative contour lines appear as the flow approaches the step (Figure 13a); this structure has developed from the less organized one downstream of the step (Figure 13b). This process reminds us of the redevelopment of the turbulent boundary layer after the reattachment point in the PBSF (Le et al., 1997; Armaly et al., 1983; Adams et al., 1984).

Recalling that the spanwise mean wall-shear stress ($\overline{\tau}_{w_z}$) is nearly zero all along the cylinder surface (Figure 3), the high spanwise wall-shear-stress fluctuation (Figure 7) implies the presence of strong streamwise vortices. In Figure 14, contours are shown of instantaneous streamwise vorticity ($\omega_s$) in the plane perpendicular to the cylinder surface at $s/h = 3.5$ at two different times; solid and dashed lines represent positive and negative values, respectively. Pairs of strong $\omega_s$ are clearly identified at any instant; similar streamwise vortices were observed in the PBSF (Figure 6 of Le et al., 1997).

Figure 15 shows instantaneous contours of the spanwise vorticity ($\omega_z$) at a typical *x-y* plane; solid and dashed lines represent positive and negative values, respectively. The elongated free shear layer is clearly noticed. Furthermore, the vortices shed from the step can also be identified near the cylinder surface at $s/h = 3$. A flow animation made from our DNS data, which is not shown here, confirms that the quasi-periodic vortex shedding is related to the behavior of the reattachment points.

### Distribution of *P*

As noted earlier, *P* in Equation (2) includes not only pressure but also the centrifugal potential; its gradient is involved in determining the velocity field. The contours of mean $P(\overline{P})$ averaged in time and *z* are presented in Figure 16. Obviously, centrifugal force is seen outside the main recirculating region. Unlike the PBSF reported in Le et al. (1997), one cannot find a favorable gradient of *P* near the step. Figure 17 shows the contours of rms of *P* fluctuation ($\sqrt{P'^2}$). The *P* fluctuations in the region close to the cylinder surface are high near the reattachment location in a broad range of *s* ($3.0 \leq s \leq 5.0$), which is consistent with the previous observation related to the
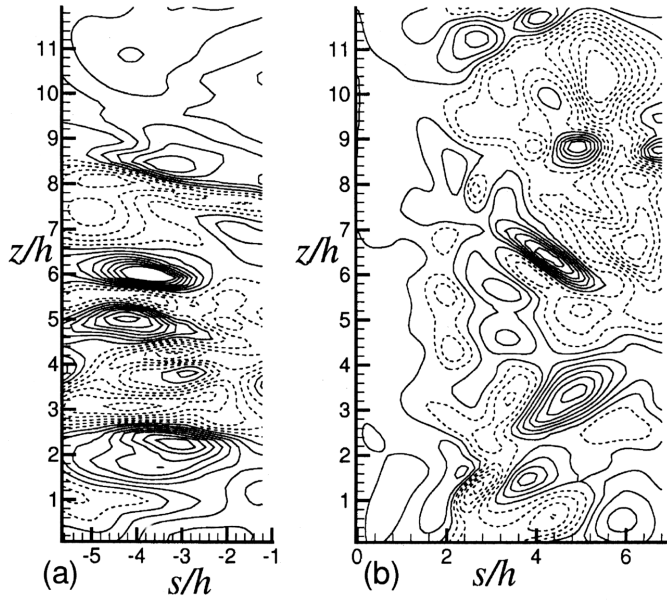
**Figure 13.** Contours of the instantaneous fluctuation of the circumferential velocity component ($u'_s$) at $0.006h$ away from the cylinder surface, normalized by $U_0$: — positive; - - - negative, $\Delta u'_s / U_0 = 0.00084$; (a) upstream of the step; (b) downstream of the step.
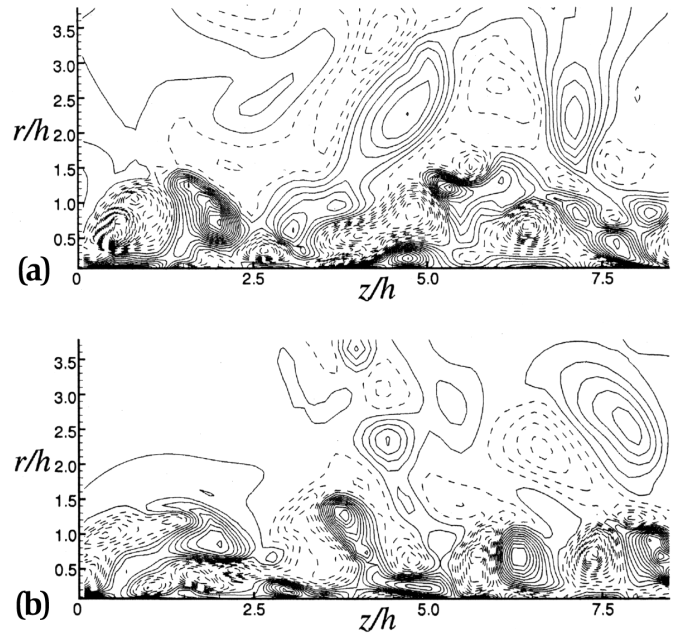


**Figure 14.** Contours of instantaneous streamwise vorticity ($\omega_s$) at $s/h = 3.5$, normalized by $U_0/h$, $\Delta\omega_s\, h/ U_0 = 0.19$; (a) $t = t_1$; (b) $t = t_1 + 3.1T$.
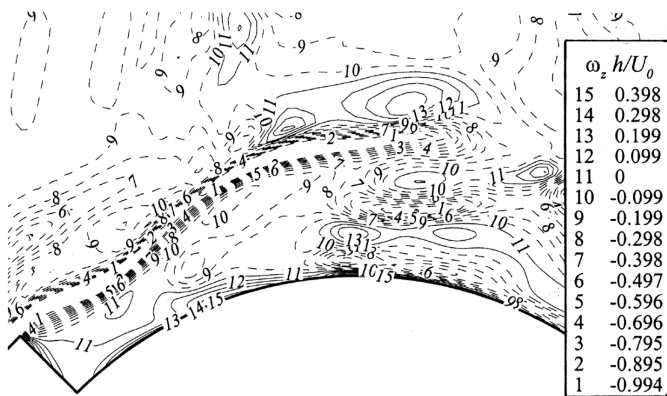


**Figure 15.** Contours of instantaneous spanwise vorticity ($\omega_z$) at a typical $x$-$y$ plane.
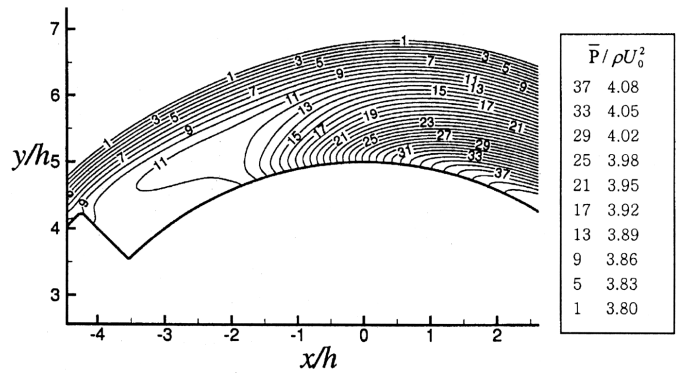


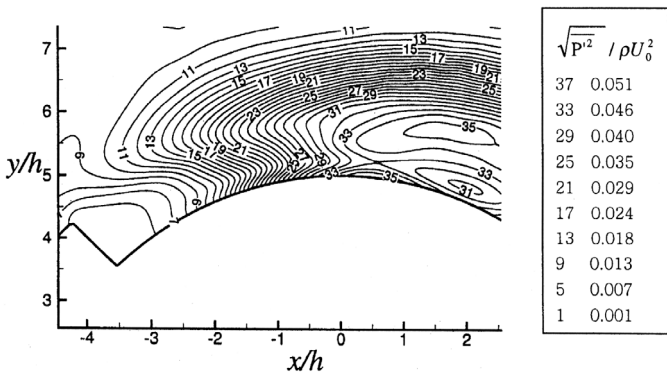**Figure 16.** Contours of the mean $P$ ($\overline{P}$) averaged in time and $z$.



**Figure 17.** Contours of rms of $P$ fluctuation, $\sqrt{P'^2}$.

region of high mass and heat transfer rates. Le et al. reported a similar trend as seen in Figure 14 of Le et al. (1997).

Unsteady motion of large-scale vortices can be identified by the contours of the spanwise-averaged $P$ fluctuations depicted in Figure 18. It clearly reveals a vortex shedding and mutual merging during a relatively short period of time ($0.08T$).

## Joint PDF of Wall-Shear-Stress Components

Statistical occurrence of $\tau_{w_s}$ and $\tau_{w_z}$ at a given $s$ can be represented by a joint probability density function (PDF, $\phi$) defined as follows (Tennekes and Lumley, 1972):

$$\phi(\tau_{w_s}, \tau_{w_z})\Delta\tau_{w_s}\Delta\tau_{w_z} = \frac{n}{N \times N_z} \tag{5}$$
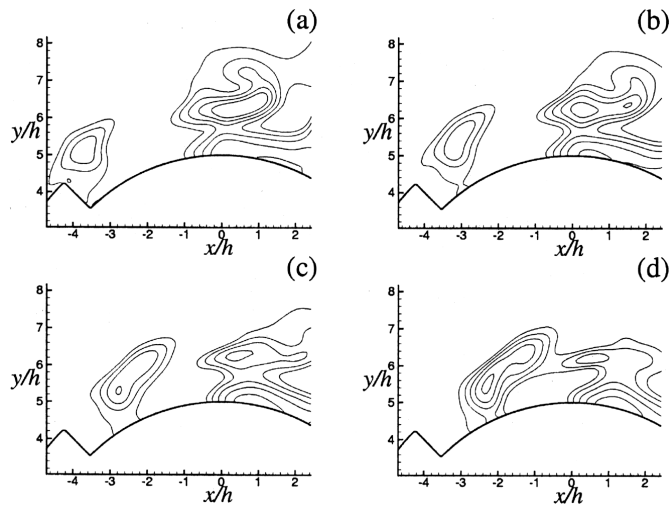
**Figure 18.** Contours of the spanwise-averaged $P$ fluctuations, $\sqrt{P'^2}/\rho U_0^2$; increment, 0.017; (a) $t = t_1$, (b) $t = t_1 + 0.027T$, (c) $t = t_1 + 0.053T$, (d) $t = t_1 + 0.08T$, where $T$ is the period of the cylinder rotation.

$$\phi(\tau_{w_s}, \tau_{w_z}) \geq 0, \qquad \int_{-\infty}^{\infty}\int_{-\infty}^{\infty} \phi(\tau_{w_s}, \tau_{w_z})\tau_{w_s}\, d\tau_{w_z} = 1 \qquad (6)$$

Here, $N$ denotes the number of instantaneous fields sampled during three revolutions of the cylinder, and $N_z$ represents spanwise samples per each instantaneous field, equivalent to the number of grid points in $z$. The number of the samples falling within a specific $\tau_{w_s}$ to $\tau_{w_z}$ range is denoted by $n$. Figure 19 shows PDFs of $(\tau_{w_s} - \tau_{w_z})$ at $s/h = 2.9$, 3.5, 4.9, and 6.1, corresponding to the circumferential locations of the maximum $|\bar{\tau}_{w_s}|$, the maximum $J$, the reattachment point, and a location $1.2h$ downstream of the reattachment point, respectively. Figure 19 reveals relatively broad and symmetric PDF distributions in all cases; this implies a weak correlation between $\tau_{w_s}$ and $\tau_{w_z}$.

One can extract more information from Figure 19. Firstly, each PDF distribution is symmetric with respect to the axis of $\tau_{w_z} = 0$; this is another indication of $\bar{\tau}_{w_z} \approx 0$. Secondly, the shape of each PDF distribution is nearly elliptic with $\tau_{w_z}$ as the major axis, illustrating that spanwise fluctuation is more severe than the circumferential one. Thirdly, in the case of $s/h = 3.5$ (Figure 19b), the values of PDF are more scattered than those of the other cases, implying a large value of $J$ at this location (Figure 7).
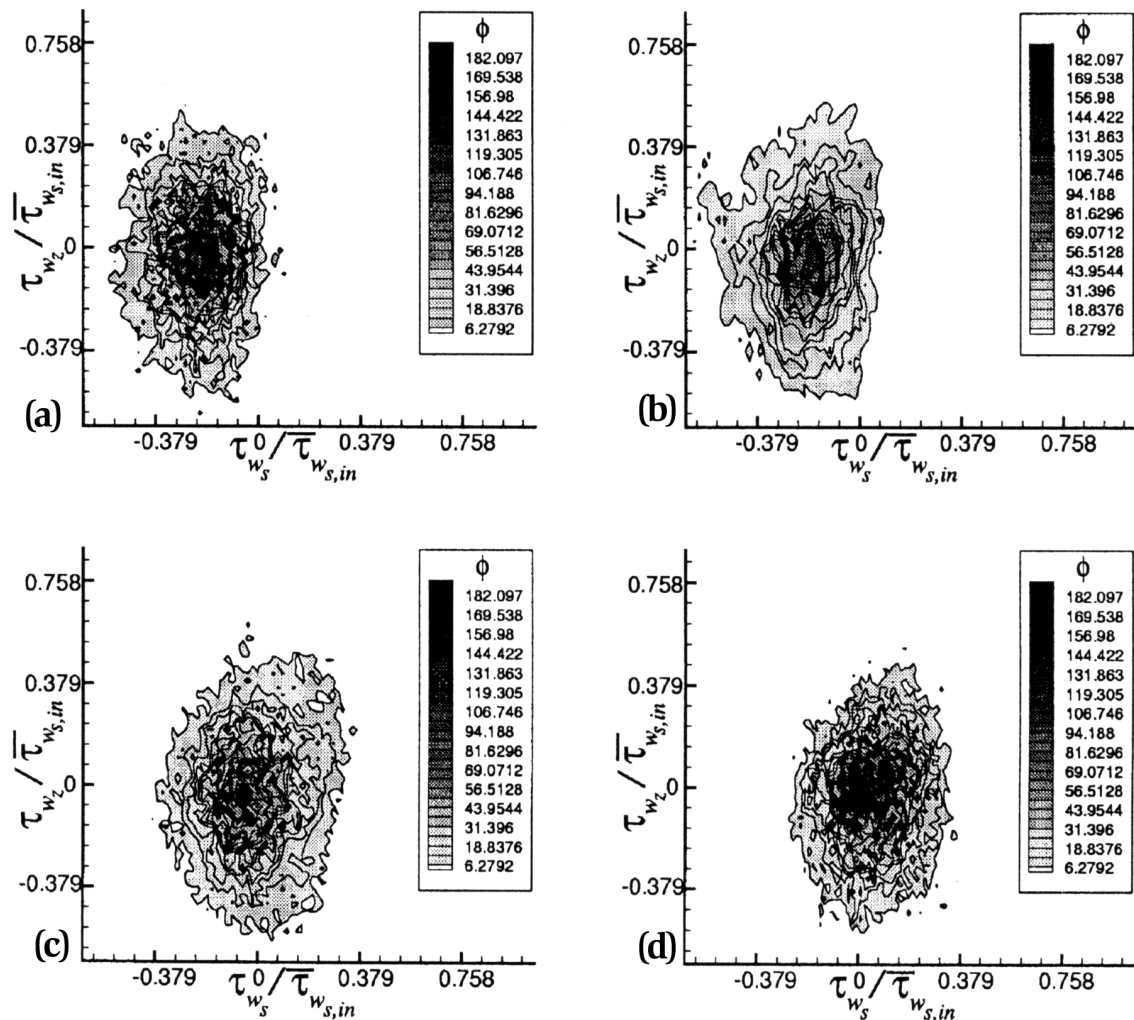


**Figure 19.** Probability Density Function of $\tau_{w_s}$ and $\tau_{w_z}$: (a) $s/h = 2.9$; (b) $s/h = 3.5$; (c) $s/h = 4.9$; (d) $s/h = 6.1$.
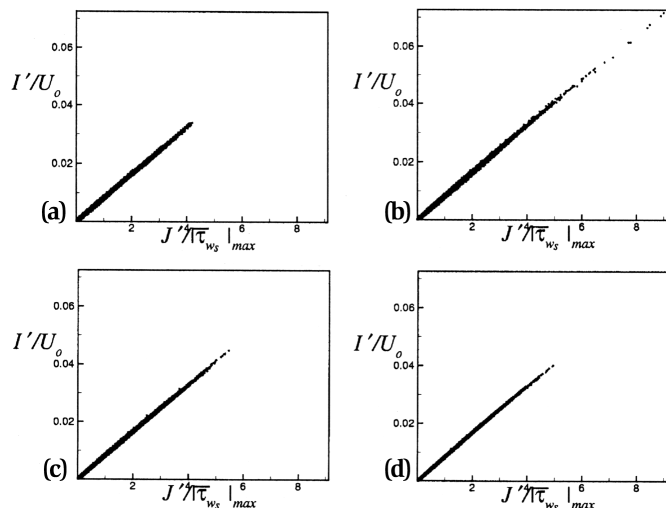
**Figure 20.** Distribution of instantaneous turbulent fluctuation ($I' = \sqrt{u'_i u'_i / 3}$) at $y = 0.006h$ and wall-shear-stress fluctuation ($J' = \sqrt{\tau'^2_{w_s} + \tau'^2_{w_z}}$); (a) $s/h = 2.9$; (b) $s/h = 3.5$; (c) $s/h = 4.9$; (d) $s/h = 6.1$.

In the previous section, it was mentioned that turbulent fluctuation ($I' = \sqrt{u'_i u'_i / 3}$) and wall-shear-stress fluctuation ($J' = \sqrt{\tau'^2_{w_s} + \tau'^2_{w_z}}$) are closely related to the mass-transfer capacity. Figure 20 shows the correlations between these two instantaneous quantities at the locations corresponding to those in Figure 19. Here, the same number of samples ($N \times N_z$) was used as in Figure 19 and $I'$ was taken at $0.006h$ away from the cylinder surface. Figure 20 confirms that in the vicinity of the cylinder surface, $I'$ is proportional to $J'$ since the wall normal component of velocity fluctuation is small compared with the other two. Furthermore, one can identify a few instants of large $I'$ and $J'$ in Figure 20b corresponding to the location of maximum $J$ (Figure 7). Such strong instantaneous fluctuations contribute to the process of erosion-corrosion, even though they do not frequently occur. To the authors' knowledge, this behavior has never been measured nor explicitly calculated previously.

## Conclusions

In this investigation, turbulent flow around a rotating cylinder with two backward-facing steps mounted axisymmetrically with respect to the axis of rotation was numerically studied using DNS. The results are presented with respect to the rotating reference frame in which the cylinder is stationary and the outer boundary is rotating. A rotational speed of 2000 rpm in air, corresponding to $Re = 335$ based on the step height and the circumferential speed of the cylinder surface, is considered. It is revealed that this flow geometry creates a qualitatively similar flow pattern, as observed near a sudden pipe expansion or a plane backward-facing step, characterized by flow separation and reattachment.

Intense turbulent fluctuation and its steep normal gradient are observed in the vicinity of the cylinder surface in the recirculating region. Strong wall-shear-stress fluctuation is also detected along the cylinder surface in a wide range of 2 to 5 step heights downstream of the step; this is consistent with the range of measured high mass-transfer rates. Since erosion-corrosion is often mass-transfer controlled, it is confirmed that turbulence effects, such as turbulent fluctuation and wall-shear-stress fluctuation, can accelerate the rate of erosion-corrosion.

## Acknowledgements

## Nomenclature

| | |
|---|---|
| $h$ | step height, (m) |
| $I$ | turbulence intensity, (m/s) |
| $I'$ | instantaneous turbulence fluctuation, (m/s) |
| $J$ | rms of instantaneous wall-shear-stress fluctuation, (Pa) |
| $J'$ | instantaneous wall-shear-stress fluctuation, (Pa) |
| $n$ | direction locally perpendicular to the outer boundary, |
| $N, N_z$ | number of instantaneous fields sampled, and samples in spanwise direction per each instantaneous field, respectively |
| $P, \overline{P}$ | sum of pressure and centrifugal potential, and mean $P$, respectively, (Pa) |
| $r_o$ | outer radius of the domain, (m) |
| $Re$ | Reynolds number |
| $s$ | coordinate axis along the cylinder surface, (m) |
| $T$ | period of the cylinder rotation, (s) |
| $\mathbf{u}$ | velocity vector, (m/s) |
| $u'_i$ | velocity fluctuation in direction $i$, (m/s) |
| $u_\tau$ | friction velocity, (m/s) |
| $U_0$ | circumferential speed of the cylinder surface upstream of the step, (m/s) |
| $U_s$ | mean circumferential velocity component, (m/s) |
| $v_\theta, v_r, v_z$ | circumferential, normal, and spanwise velocity components, respectively, (m/s) |
| $W$ | spanwise size of the domain, (m) |
| $x, y, z$ | Cartesian coordinates, (m) |
| $X_r$ | mean reattachment length, (m) |

### Greek Symbols

| | |
|---|---|
| $\nu$ | kinematic viscosity, (m$^2$/s) |
| $\rho$ | density, (kg/m$^3$) |
| $\overline{\tau}_w$ | averaged wall-shear stress, (Pa) |
| $\tau'_w$ | wall-shear-stress fluctuation, (Pa) |
| $\phi$ | joint probability density function, (PDF, Pa$^{-2}$) |
| $\omega_s, \omega_z$ | streamwise, and spanwise vorticity, respectively, (s$^{-1}$) |
| $\Omega$ | angular velocity, (s$^{-1}$) |

## References

Adams, E.W., J.P. Johnston and J.K. Eaton, "Experiments on the Structure of Turbulent Reattaching Flow", Rep. MD-43, Thermosciences Division, Department of Mechanical Engineering, Stanford University, Palo Alto, CA (1984).

Armaly, B.F., F. Durst, J.C.F. Pereira and B. Schönung, "Experimental and Theoretical Investigation of Backward-Facing Step", J. Fluid Mech. **127**, 473–496 (1983).

Bienkowski, J., "A Rotating Cylinder Electrode with Surface Roughness", Honours Thesis, Department of Mechanical Engineering, The University of Queensland, Brisbane, Australia (1998).

Calmet, I. and J. Magnaudet, "Large-Eddy Simulation of High-Schmidt Number Mass Transfer in a Turbulent Channel Flow", Physics of Fluids **9**, 438–455 (1997).

Campbell, J.A. and T.J. Hanratty, "Mechanism of Turbulent Mass Transfer at a Solid Boundary", AIChE J. **29**, 221–229 (1983).

Elvery, D.G. and K. Bremhorst, "Wall Pressure and Effective Wall Shear Stress in Heat Exchanger Tube Inlets with Application to Erosion-Corrosion", Trans. ASME, Journal of Fluids Engineering **119**, 948–953 (1997).

Elvery, D.G. and K. Bremhorst, "Erosion-Corrosion Due to Inclined Flow into Heat Exchanger Tubes – Investigation of Flow Field"

Proceedings of the ASME Fluids Engineering Division Summer Meeting, San Diego, California, U.S.A. July 7–11, FED-**237**, 595–600 (1996).

Härtel, C., "Turbulent Flows: Direct Numerical Simulation and Large-Eddy Simulation", in "Handbook of Computational Fluid Mechanics", Chapter 5, Academic Press, New York, NY (1996), pp. 283–338.

Le, H., P. Moin and J. Kim, "Direct Numerical Simulation of Turbulent Flow over a Backward-Facing Step", J. Fluid Mech. **330**, 349–374 (1997).

Lezius, D.K. and J.P. Johnston, "Roll-Cell Instabilities in Rotating Laminar and Turbulent Channel Flows", J. Fluid Mech. **77**, 153–175 (1976).

Mahato, B.K., S.K. Voora and L.W. Shemilt, "Steel Pipe Corrosion Under Flow Conditions – I. An Isothermal Correlation for a Mass Transfer Model", Corros. Sci. **8**, 173–193 (1968).

Nesic, S., J. Bienkowski, K. Bremhorst and K.-S. Yang, "Testing for Erosion-Corrosion Under Disturbed Flow Conditions using a Rotating Cylinder with a Stepped Surface", Corrosion **56**, 1005–1014 (2000).

Nesic, S. and J. Postlethwaite, "Relationship between the Structure of Disturbed Flow and Erosion-Corrosion", Corrosion **46**, 874–880 (1990).

Postlethwaite, J.M., H. Dobbin and K. Bergevin, "The Role of Oxygen Mass Transfer in the Erosion-Corrosion of Slurry Pipelines", Corrosion **42**, 514–521 (1986).

Postlethwaite, J. and S. Nesic, "Erosion-Corrosion in Single and Multiphase Flow", Uhlig Corrosion Handbook, 2nd edition, Edited by W. Revie, Ed., John Wiley and Sons Inc., New York, NY (2000), pp. 249–272.

Rosenfeld, M., D. Kwak and M. Vinokur, "A Fractional Step Solution Method for the Unsteady Incompressible Navier-Stokes Equations in Generalized Coordinate Systems", Journal of Computational Physics **94**, 102–137 (1994).

Silverman, D.C., "Rotating Cylinder Electrode-Geometry Relationships for Prediction of Velocity-Sensitive Corrosion", Corrosion-NACE **44**, 42–49 (1988).

Tennekes, H. and J.L. Lumley, "A First Course in Turbulence", The MIT Press, Cambridge, MA (1972).